Frequency-Bessel Transform Method for Effective Imaging of Higher-Mode Rayleigh Dispersion Curves From Ambient Seismic Noise Data

Jiannan Wang[1], Gaoxiong Wu[1,2], and Xiaofei Chen[2]

[1]School of Geophysics, School of Earth and Space Sciences, University of Science and Technology of China, Hefei, China, [2]Department of Earth and Space Sciences, Southern University of Science and Technology, Shenzhen, China

Correspondence to: Xiaofei Chen, chenxf@sustc.edu.cn

Abstract

It has been widely recognized that the cross-correlation function of ambient seismic noise data recorded at two stations approximates to the part of Greens function between two stations. Therefore, the cross-correlation function should include higher modes, aside from the fundamental mode. However, the problem of measuring or extracting overtones from ambient seismic noise data remains. In this paper, we propose the frequency-Bessel transform method (F-J method) for extracting the dispersion curves of higher modes from ambient seismic noise data. We then assess the validity, accuracy, and applicability of the F-J method by conducting extensive numerical simulations and processing the observed ambient seismic noise data of the USArray. As demonstrated in this study, the F-J method is a convenient, practical, and accurate method for extracting the dispersion curves of multimodes from ambient seismic noise data and therefore has significant potentiality in the field of ambient seismic noise tomography.

1 Introduction

Ambient seismic noise, which is also called microtremor in the field of geotechnique engineering, is a stochastic wavefield generated by various passive sources (e.g., Okada & Suto, 2003; Yang et al., 2007; Yang & Ritzwoller, 2008). After the pioneering works of Aki (1957) and other researchers (e.g., Campillo & Paul, 2003; Derode et al., 2003; Lobkis & Weaver, 2001; Sabra et al., 2005a, 2005b; Sánchez-Sesma et al., 2011; Shapiro & Campillo, 2004; Shapiro et al., 2005; Snieder, 2004), once useless ambient noise data were converted to useful seismic data from which the group and/or phase velocity of surface waves can be extracted. Consequently, a new field of ambient seismic noise surface tomography quickly emerged and is widely used in mapping geological structures with various scales, from shallow structure for geotechnique engineering applications to the crustal and lithospheric structure (e.g., Bensen et al., 2007, 2009; Lin et al., 2008; Moschetti et al., 2007; Nakamura, 1989; Nishida et al., 2009; Okada & Suto, 2003; Satoh et al., 2001; Shapiro et al., 2005; Shen & Ritzwoller, 2016; Taylor et al., 2009; Tokimatsu, 1997; Yang & Ritzwoller, 2008; Yao et al., 2006).

The ambient noise cross-correlation method provided an effective tool for measuring phase/group velocity in a relatively shorter period than conventional seismic surface wave method. Thus, it significantly improved the resolution of seismic surface wave tomography and extended its applicability (e.g., Bensen et al., 2009; Lin et al., 2011; Tian et al., 2013; Yang & Ritzwoller, 2008; Yang et al., 2011). However, it still suffers from similar problems as encountered by the classic surface wave tomography method, such as nonuniqueness and limited accuracy in inverting crustal and lithospheric structure. Nonuniqueness occurs because only the fundamental dispersion curve is used in the inversion. Therefore, extracting the dispersion curves of overtones and using them in the inversion are crucial for resolving or reducing nonuniqueness and increasing the accuracy of surface wave inversion. This notion has long been recognized in the study of surface wave tomography (e.g., Asten, 2006; Maraschini et al., 2010; Nolet & Panza, 1976; Wiggins, 1972; Yokoi, 2010).

Extracting dispersion curves from ambient noise is a key step in microtremor survey and ambient seismic noise tomography. A number of methods have been developed during the past few decades, such as the spatial autocorrelation method (Aki, 1957), the frequency wave number (FK) method (Capon, 1969; Lacoss et al., 1969), the phase velocity image analysis (Yao et al., 2006), the multichannel analysis of surface wave (MASW) method (e.g., Park et al., 1998, 2007; Park & Miller, 2008), and the high-resolution linear Radon transform (e.g., Luo et al., 2008; Pan et al., 2016). Methods for extracting the fundamental dispersion curve are considered mature. Recently, more and more researchers identified the higher modes from ambient seismic noise through careful analysis for certain cases (e.g., Brooks et al., 2009; Gualtieri et al., 2015; Harmon et al., 2007; Kimman & Trampert, 2010; Lin et al., 2013; Mordret et al., 2014; Nishida et al., 2008; Rivet et al., 2015; Savage et al., 2013; Tomar et al., 2018; Yao et al., 2011).

In this paper, we propose a new method called *frequency-Bessel method* (abbreviated as F-J method) for extracting the dispersion curves of overtones. Its validity, accuracy, and applicability are systematically investigated through a variety of synthetic data. We also test this new method by applying it to the observed ambient seismic noise data of USArray.

2 Theory of Frequency-Bessel Transform Method

In a flat multilayered isotropic elastic model, consider that ambient seismic noise is a stochastic field, which is stationary in space and time. The temporal cross-correlation function (CCF) of ambient seismic noise records between two receivers is defined as (e.g., Jacobson, 1962)

$$C(\mathbf{r},t)=\int_0^T \langle u(\mathbf{x}_1,\tau-t)u(\mathbf{x}_2,\tau)\rangle \,\mathrm{d}\tau, \quad (1)$$

where $u(x,t)$ is a vertical component of ambient seismic noise recording in point x and $r = x_1 - x_2$. $\langle\cdot\rangle$ denotes the average over the stochastic ensemble. According to the equipartition assumption (Campillo & Paul, 2003; Sanchezsesma & Campillo, 2006), the ambient seismic noise is an isotropic field, such that $C(r,t) = C(r,t)$, $r = |r|$ is the distance between two stations. In frequency domain, formula 1 becomes

$$\tilde{C}(r,\omega) = \langle [\tilde{u}(\mathbf{x}_1,\omega)]^* \tilde{u}(\mathbf{x}_2,\omega) \rangle, \quad (2)$$

where $\tilde{C}(r,\omega) = F[C(r,t)]$, $\tilde{u}(x,\omega) = F[u(x,t)]$ and "$*$" denotes the complex conjugate. Then, we define the frequency vector wave number transformation to the spectrum of CCF $\tilde{C}(r,\omega)$ as follows:

$$I(\omega,\mathbf{k}) = \frac{1}{2\pi} \int_{-\infty}^{+\infty} \int_{-\infty}^{+\infty} \tilde{C}(r,\omega) e^{j\mathbf{k}\cdot\mathbf{r}} \, \mathrm{d}\Sigma(\mathbf{r}). \quad (3)$$

This integration is performed over the entire surface. In a cylindrical coordinate system, equation 3 becomes

$$I(\omega,k) = \frac{1}{2\pi} \int_{0}^{+\infty} \int_{0}^{2\pi} \tilde{C}(r,\omega) e^{jkr\cos(\theta)} r \, \mathrm{d}\theta \mathrm{d}r, \quad (4)$$

where $k = |k|$. By using the integral representation of the Bessel functions (e.g., Temme, 1996),

$$\frac{1}{2\pi} \int_{0}^{2\pi} e^{jkr\cos(\theta)} \, \mathrm{d}\theta = J_0(kr), \quad (5)$$

equation 4 can be simplified to

$$I(\omega,k) = \int_{0}^{+\infty} \tilde{C}(r,\omega) J_0(kr) r \, \mathrm{d}r. \quad (6)$$

Equation 6 reveals that for isotropic CCF, the vector wave number (two-dimensional) can be reduced to a one-dimensional integral and depends only on the norm of the vector wave number (k) rather than vector k. Noticed that $I(\omega,k)$ is a simplified frequency-Bessel transform. For this reason, we will use $I(\omega,k)$ instead of $I(\omega,k)$ hereafter in this paper and name it the *frequency-Bessel spectrogram* (abbreviated as F-J spectrogram).

According to previous studies (e.g., Sanchezsesma & Campillo, 2006; Sato et al., 2012), the Fourier transform of the CCF of ambient seismic noise data between two points is approximate to the imaginary part of Green's function between these points, that is,

$$\tilde{C}(r,\omega) \approx A \cdot Im\left\{\tilde{G}_{zz}(r,z=0,;\omega)\right\}, \quad (7)$$

where A is a constant and $\tilde{G}_{zz}(r,z=0;\omega)$ is a spectrum of vertical component of Green's function with hypocentral distance r and recorded at the surface ($z = 0$).

For a flat-layered elastic half space, Green's function due to an isotropic source (e.g., explosive and vertically vibrating source) presents with the following form (e.g., Chen, 1993, 1999; Hisada, 1994; Kennett, 1986; Luco & Apsel, 1983):

$$\tilde{G}_{zz}(r, z=0;\omega) = \int_0^{+\infty} g_z(z=0,\kappa,\omega) J_0(\kappa r)\kappa \,\mathrm{d}\kappa, \quad (8)$$

where $g(z,\kappa,\omega)$ is a kernel function that is independent of r. In addition, $J_0(kr)$ is the first kind of the Bessel function of zero order.

Substituting equations 7 and 8 into equation 6 yields

$$I(\omega,k) \approx A \int_0^{+\infty}\int_0^{+\infty} Im\{g_z(z=0,\kappa,\omega)\} J_0(\kappa r) J_0(kr) r\kappa \,\mathrm{d}\kappa \,\mathrm{d}r. \quad (9)$$

By exchanging integration orders and using the orthogonal property of Bessel function (e.g., Arfken et al., 2012): $\int_0^{+\infty} J_0(kr)J_0(\kappa r) r\,\mathrm{d}r = \frac{1}{\kappa}\delta(k-\kappa)$, the above equation can be reduced to

$$I(\omega,k) \approx A \int_0^{+\infty} Im\{g_z(z=0,\kappa,\omega)\} \left\{\delta(\kappa-k)\frac{1}{\kappa}\right\} \kappa \,\mathrm{d}\kappa. \quad (10)$$

Lastly, we obtain

$$I(\omega,k) \approx A \cdot Im\{g_z(z=0,k,\omega)\}. \quad (11)$$

In terms of ω and c, ($c = \omega/k$, c is phase velocity), the above equation can be recast as

$$I(\omega,c) \approx A \cdot Im\{g_z(z=0,c,\omega)\}. \quad (12)$$

We see that $I(\omega,c)$ can be accurately computed using equation 6 through integration. In practice, however, we cannot obtain such an exact $I(\omega,c)$ because of only limited available data for evaluating the integral. For instance, we only have data $\{\tilde{C}(r_j,\omega), j=1,2,\ldots,N\}$. As shown in the Appendix Appendix A, with use of the limited available seismic data from the observation array, we can obtain an approximate $I(\omega,c)$ through a finite discrete summation:

$$I(\omega,c) \approx \sum_{j=1}^{N} \left\{ \left(\frac{c}{\omega}\right)\tilde{C}(r_j,\omega) r_j J_1\left(\frac{\omega}{c}r_j\right) + b_j\left(\frac{c}{\omega}\right)^3 \left[\frac{\omega}{c} r J_0\left(\frac{\omega}{c}r\right) - B_0\left(\frac{\omega}{c}r\right)\right] \right\} \Big|_{r_{j-1}}^{r_j}, \quad (13)$$

where r_j is distance between the jth pair stations from which the CCF $\tilde{C}(r_j,\omega)$ is calculated, with definition $r_0 = 0$, function $B_0(x) = \int_0^x J_0(\eta)\,\mathrm{d}\eta$, and coefficient b_j given by $b_j = [\tilde{C}(r_j) - \tilde{C}(r_{j-1})]/\delta r_j$.

We note that the kernel function $g_z(z=0,c,\omega)$ is inversely proportional to the secular function $\det|\mathbf{I} - \mathbf{R}_D^{sl}\mathbf{R}_U^{fs}|$ (I is an identity matrix; R is the reflection matrix; subscripts D and U denote the downgoing and upgoing; s,l, and f denote the source, half-space boundary, and free surface, respectively; e.g.,

Kennett, 1986; McMechan & Yedlin, 1981). Obviously, the dispersion points ($c = c_n(\omega), n = 0,1,2,\ldots$), which are the roots of the secular function, are singular points of the kernel function. Therefore, kernel function $g_z(z = 0,c,\omega)$ tends to infinity at dispersion points. Figure 1 shows an example of $Im\{g_z(z = 0,c,\omega)\}$ in the "f-c" domain for a given flat-layered model whose parameters are shown in Table 1. The black dotted lines are the theoretically predicted dispersion curves, which perfectly match the areas with a large value of the imaginary part of kernel function. Theoretically, the values of kernel function at dispersion points should be infinity. Due to the finite pixel scanning, only finite though larger values can be observed in plotting $Im\{g_z(z = 0,c,\omega)\}$. According to this singular property of kernel function, we propose a new method for extracting the dispersion curves from array ambient noise data. This new method mainly consists of the following steps:

Step 1.For a given seismographic observation array, the spectral CCFs for all possible station pairs are calculated after performing the preprocessing of the ambient seismic noise records. This step is same as the preprocessing procedure in ambient seismic noise surface wave tomography (e.g., Bensen et al., 2007; Lin et al., 2008; Prieto et al., 2011; Shapiro & Campillo, 2004; Yao et al., 2006).

Step 2.Sort spectral CCFs as a function of interstation distance (r_j) and conducting frequency-Bessel transform to them, that is, calculating the F-J spectrogram $I(\omega,c)$ by the discrete summation formula for each given ω.

Step 3.Identify the dispersion curves from the $I(\omega,c)$ image with the help of an image recognition algorithm.

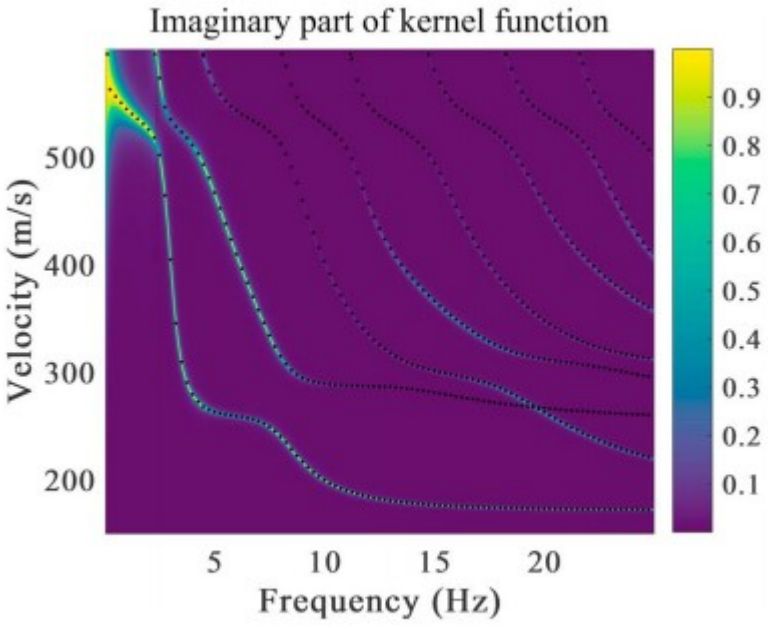

Figure 1. The imaginary part of kernel function $g_z(0, c, \omega)$ of model 1. Black dotted lines denote theoretical dispersion curves.

Table 1
Parameters of Model 1

Depth (m)	Density (kg/m^3)	*S* wave velocity (m/s)	*P* wave velocity (m/s)	*Q* value
0	1,780	180	1,500	10,000
10	1,850	350	1,700	10,000
20	1,800	250	1,600	10,000
40	1,940	600	2,000	10,000

We thus name this new method the *frequency-Bessel transform method*, abbreviated as F-J method. Our new method is similar to but different from the MASW (Park & Miller, 2008; Park et al., 2007) and Radon transform method (e.g., Luo et al., 2008; Pan et al., 2016; in short RTM). In MASW and RTM, the base function of transformation is "e^{ikx}" or "$e^{i\omega px}$," thus represents a one-dimensional spatial Fourier transformation. While in F-J method, the base function of the vector wave number transformation is "$rJ_0(kr)$." This represents an isotropic two-dimensional spatial Fourier transformation though only one-dimensional transform integration involved. The former 1-D wave number transform, or Radon transform, corresponds a 2-D wave propagation problem in a horizontally layered medium or, physically, a wave propagation problem excited by an infinite-long line source. However, the 2-D wave number transformation involved in the F-J method corresponds a 3-D wave propagation problem in a horizontally layered medium or wave propagation problem excited by a point source in horizontally layered

medium. Almost all real problems encountered in our studies are 3-D problems; therefore, F-J method is an appropriate choice.

3 Tests With Synthetic Data

To assess the validity and accuracy of the F-J method, several numerical tests were conducted. First, the ambient seismic noise data were generated by synthesizing a vast number of theoretical seismograms for a given flat-layered model whose dispersion curves can be calculated independently (Chen, 1993). Since the F-J method is independent of scale, we only synthesize ambient seismic noise data for models with small scale. Second, we applied the F-J method to these synthetic ambient noise data to image the dispersion curves for assessing the validity and accuracy of F-J method.

3.1 Synthetic Ambient Seismic Noise Data

We follow the method (Bonnefoy-Claudet et al., 2004) to synthesize ambient noise data; 1,000 sources were randomly distributed on the surface within a ring zone that spans 500 to 1,500 m, as shown in Figure 2a. Each source is a vertical point force with a Ricker wavelet. The center frequencies of the sources are randomly distributed between 6 and 10 Hz, as shown in Figure 2b. The force intensities are also randomly distributed between 0.001 and 1, as shown in Figure 2c. The vertical components of the synthetic ambient noise are calculated for approximately 60 s with a frequency band of 0.5 to 25 Hz. We employed the generalized reflection-transmission coefficient method (e.g., Chen, 1993, 1999; Chen & Zhang, 2001; Hisada, 1994; Zhang et al., 2003) to calculate the synthetic seismograms. Figure 2d shows segment of simulated ambient noise records. Three types of observation arrays are considered in this study: linear array, trilines array, and randomly distributed array, as shown in Figure 3.

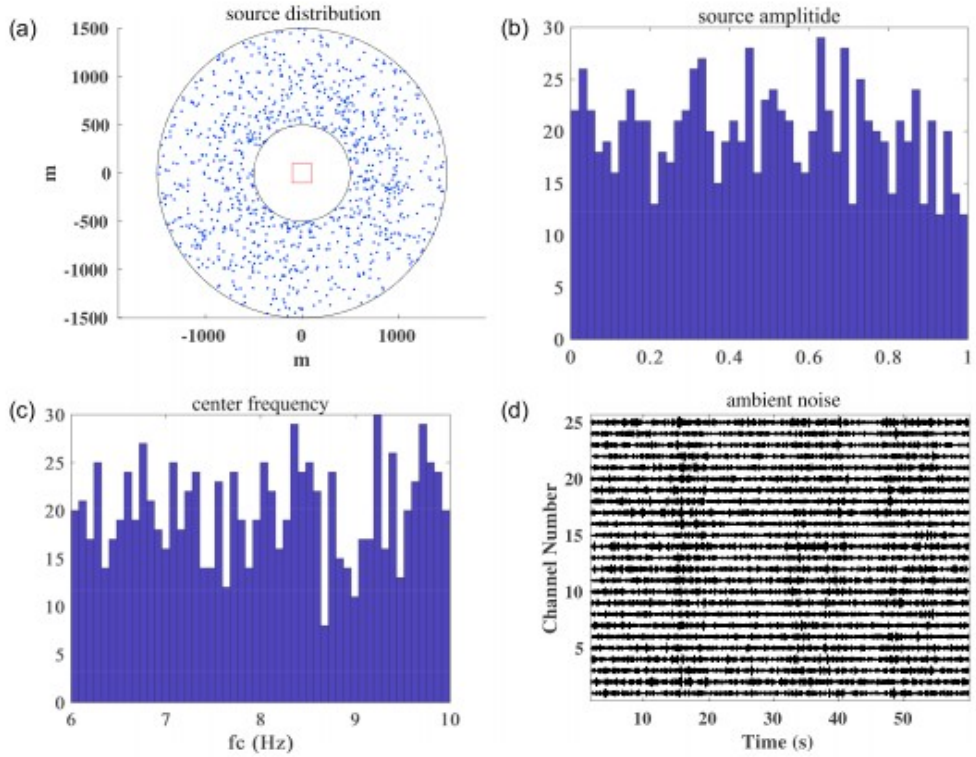

Figure 2. (a) Source distribution for generating synthetic noise data; the red box is the area where the receivers distribute. (b) Center frequency histogram for generating synthetic noise data. (c) Force intensity histogram for generating synthetic noise data. (d) Segment of simulated ambient noise records.

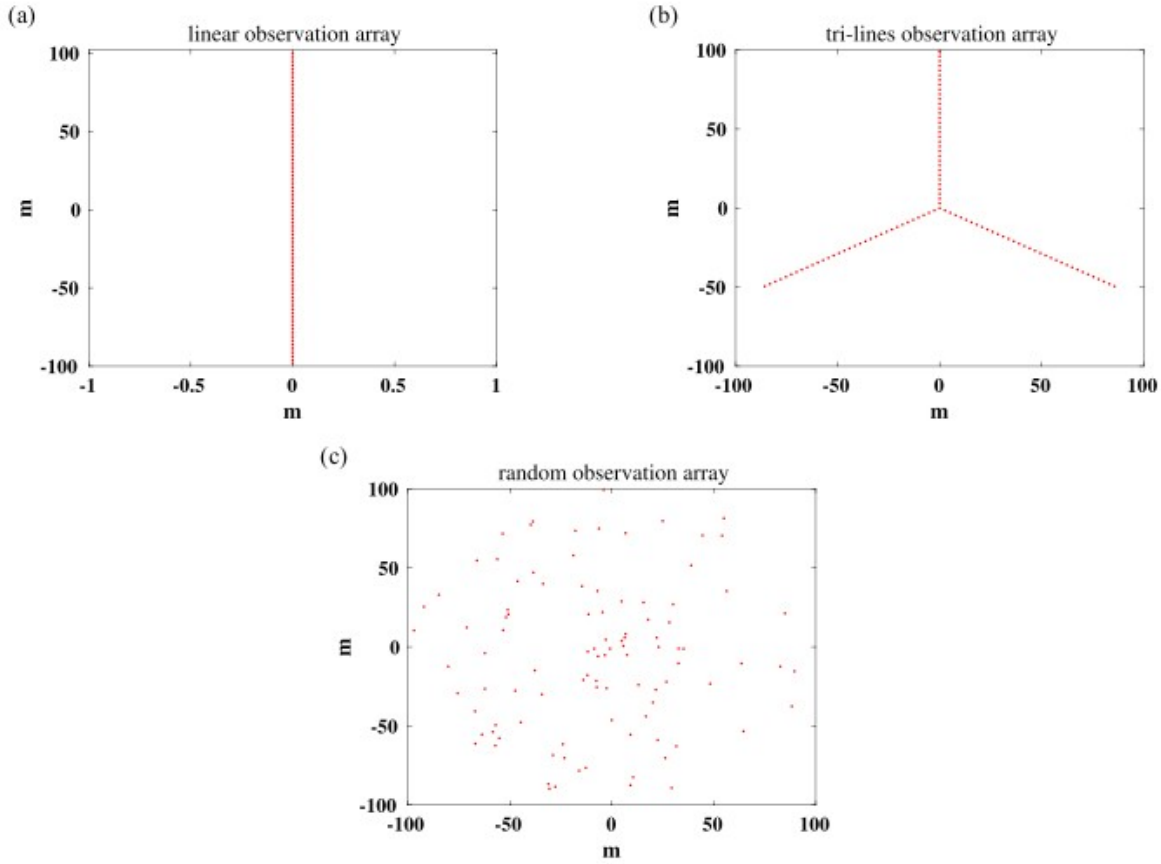

Figure 3. Observation arrays for numerical tests. (a) Linear observation array. (b) Trilines observation array. (c) Random observation array.

3.2 Structure With Soft Layers

The first model (referred model 1 hereafter) for the numerical test consists of four layers with a low-velocity zone (Table 1; Ikeda et al., 2012). Three observation arrays are investigated. The imaginary part of kernel function $Im\{g_z(0,c,\omega)\}$ for this velocity model is computed and displayed in Figure 1, in which dispersion curves are indicated by black dotted lines. We see that the kernel function perfectly matches the theoretical dispersion curves. In addition, the energy of the first mode dominates at two frequency ranges, namely, 4–9 and 19–25 Hz. In 13- to 17-Hz range, additional higher mode dispersion curves appear.

3.2.1 Linear Observation Array

In the linear observation array, 100 receivers are equally distributed along a line, as shown in Figure 3a. The total extent of array is 200 m, with 2-m intervals between receivers. Synthetic ambient noise data are generated using the procedure described in section 3.1. After scanning over (ω,c), the F-J spectrogram $I(\omega,c)$ is obtained by applying the F-J method, as shown in Figure 4a.

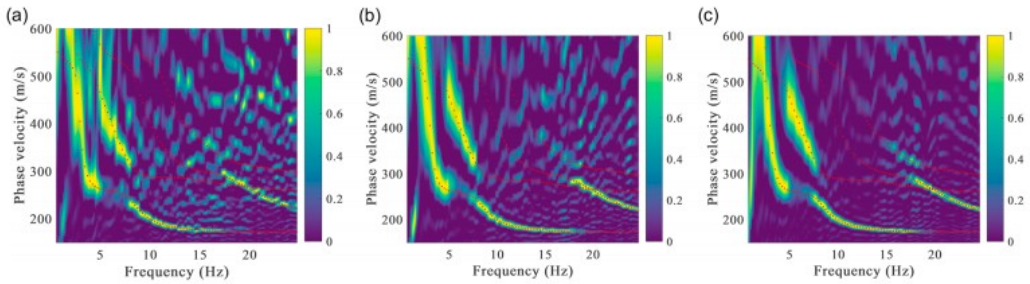

Figure 4. The F-J spectrograms $I(\omega, c)$ of model 1 using the F-J method. (a) The F-J spectrogram calculated from linear array simulated ambient noise data. (b) The F-J spectrogram calculated from trilines array simulated ambient noise data. (c) The F-J spectrogram calculated from random array simulated ambient noise data. Red dotted lines represent the theoretical dispersion curves.

As seen in Figure 4a, we can extract the dispersion curves of multimodes by tracing the peak points of the $I(\omega,c)$ image. The fundamental mode dispersion curve appears in frequency ranges of 4–5 and 7–17 Hz. The first higher mode dispersion curve appears in frequency ranges of 5–8 and 20–24 Hz, and a further higher mode appears in a frequency range of 18–20 Hz. These dispersion curves perfectly match the theoretical dispersion curves calculated using the generalized reflection-transmission coefficient method (Chen, 1993).

3.2.2 Trilines Observation Array

In this observation array, 100 receivers are equally distributed in three radiative lines from the center point, as shown in Figure 3b. The angle between any two lines is 120°, with consistent 3-m intervals between receivers along each line. The maximum radius from the center point is 99 m. We apply the F-J method to synthetic ambient noise data to obtain the F-J spectrogram $I(\omega,c)$, as displayed in Figure 4b.

By tracing the peak points of the $I(\omega,c)$ image shown in Figure 4b, we can determine not only the fundamental mode dispersion curve in frequency ranges of 3–5 and 7–20 Hz but also the first higher-mode dispersion curve in frequency ranges of 4–9 and 20–25 Hz. These dispersion curves, although only partial segments, agree well with theoretical dispersion curves plotted as red dotted lines. Another interesting feature shown on the image $I(\omega,c)$ is that the clearly recognized segments of the dispersion curves correlate well to the areas with large values of the kernel function $Im\{g_z(0,c,\omega)\}$, as shown in Figure 1.

3.2.3 Random Observation Array

The third observation array is a random array in which the receivers are randomly distributed over an area. We now investigate the effectiveness of the F-J method in this random observation array. Figure 3c shows the configuration of the observation array to be investigated. One hundred receivers were randomly distributed within a circle with a radius of 100 m.

Similarly, we apply the F-J method to synthetic ambient noise data and obtain an image of $I(\omega,c)$, as shown in Figure 4c. In this image, the

fundamental dispersion curve in the 3- to 5-Hz and 7- to 20-Hz frequency ranges can be clearly identified, whereas the dispersion curve of the first higher mode can be well determined in the 4- to 9-Hz and 20- to 25-Hz frequency ranges. We can also distinguish the dispersion curves of the overtones in other frequency ranges, such as those of the second and third modes in the 16- to 20-Hz and 15- to 18-Hz frequency ranges, respectively. We note that "osculation" seemed to occur between the first and second modes at 19 Hz, as shown in Figure 4c (e.g., Boaga et al., 2013; De Nil, 2005; Malischewsky et al., 2008; Tuan et al., 2011; Zhang & Chan, 2003; Zhang & Lu, 2003; Zhang et al., 2016). The two modes do not cross, but their phase velocity are very close to each other at this frequency.

Further comparison of the results in Figures 4a–4c shows that the dispersion curves obtained by the F-J method with a randomly distributed observation array are better than those of the linear and trilines arrays. Therefore, we shall implement the F-J method with the random observation array in the following tests.

3.3 Monotonically Increasing Velocity Model

Model 2 is a four-layer monotonically increasing velocity model (Foti et al., 2014). Table 2 displays the parameters of the model. Figure 5a plots the corresponding kernel function $Im\{g_z(0,c,\omega)\}$ of this model. Receiver distribution is same as that of the random observation array for model 1. By applying the F-J method to the synthetic noise data, we obtain the image of $I(\omega,c)$, as shown in Figure 5b. The dispersion curves of the fundamental mode for a frequency less than 15 Hz and the first higher mode within a frequency range of 15 to 25 Hz can be clearly seen on the image, which are consistent with the kernel function map (Figure 5a).

Table 2
Parameters of Model 2

Depth (m)	Density (kg/m^3)	S wave velocity (m/s)	P wave velocity (m/s)	Q value
0	1,900	100	200	10,000
5	1,900	200	400	10,000
15	1,900	300	600	10,000
30	1,900	400	800	10,000

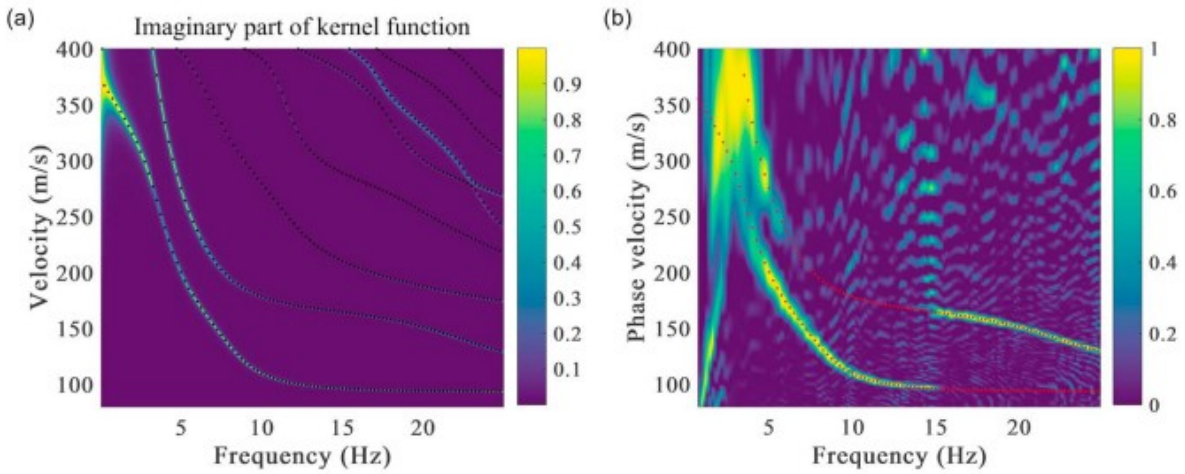

Figure 5. (a) The imaginary part of kernel function $g_z(0, c, \omega)$ of model 2. Black dotted lines denote theoretical dispersion curves. (b) The F-J spectrogram $I(\omega, c)$ of model 2 using the F-J method from random array simulated ambient noise data. Red dotted lines represent the theoretical dispersion curves.

3.4 Realistic 1-D Velocity Model

Model 3 is a 1-D velocity model based on actual near-surface sandstone and silty loam structure in Shanghai, which contains six layers. Table 3 shows the parameters of this model. Figure 6a shows the imaginary part of kernel function map of model 3. The observation array is the same as that for the problem in model 2. Furthermore, Figure 6b presents the image of $I(\omega,c)$, which was obtained by applying the F-J method to the noise data. Once again, the multimode Rayleigh dispersion curves can be clearly identified in $I(\omega,c)$ image: The fundamental mode dispersion curve appears in frequencies lower than 10 Hz, and the first, second, third, fifth, and sixth higher-mode dispersion curves appear in frequencies higher than 8, 11, and 16 Hz and within frequency ranges of 14–20 and 19–24 Hz, respectively.

Table 3
Parameters of Model 3

Depth (m)	Density (kg/m^3)	*S* wave velocity (m/s)	*P* wave velocity (m/s)	*Q* value
0	1,600	125	200	10,000
3.5	1,850	128	250	10,000
6.1	1,670	130	300	10,000
10.8	1,820	142	350	10,000
17.2	1,940	188	500	10,000
20.0	1,890	360	700	10,000

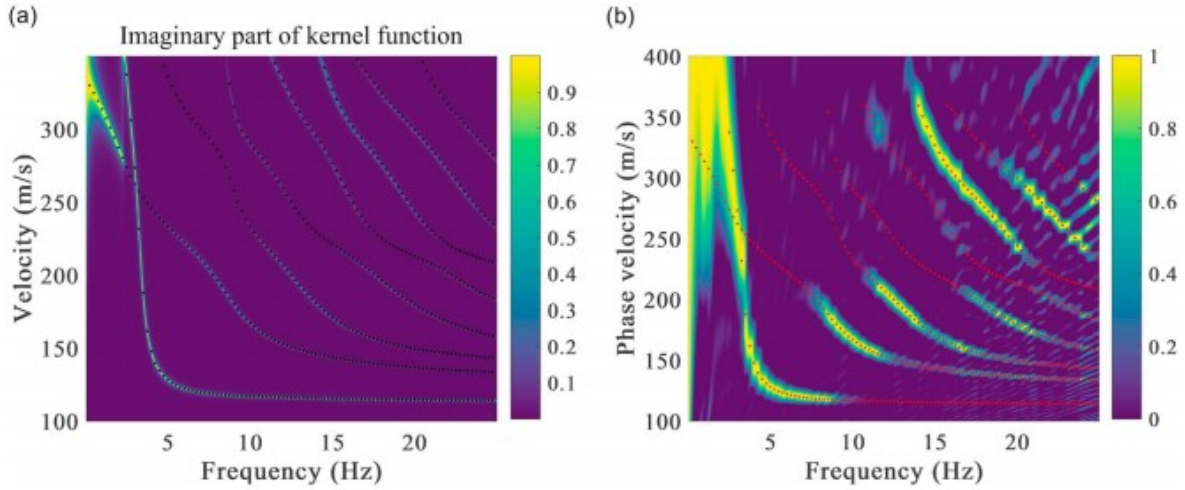

Figure 6. (a) The imaginary part of kernel function $g_z(0, c, \omega)$ of model 3. Black dotted lines denote the theoretical dispersion curves. (b) The F-J spectrogram $I(\omega, c)$ of model 3 using the F-J method from random array simulated ambient noise data. Red dotted lines represent the theoretical dispersion curves.

4 Preliminary Applications to USArray Data

We now apply the F-J method to the USArray data recorded at an area of central United States, with latitude ranging from 35° to 43° and longitude from −97° to −88°, as shown in Figure 7a. We select the high broadband vertical data data of 147 USArray Transportable array stations recorded from 1 June 2011 to 1 December 2011, a total of 183 days. We apply a band-pass filter in period band 2–50 s to 1-day data segment. Subsequently, to reduce the effect of inhomogeneous distribution of ambient seismic field source, earthquake events and instrumental irregularities, preprocessings, such as temporal normalization, spectral whitening, are performed to the raw ambient seismic noise data before computing the cross-correlation (Bensen et al., 2007). Daily CCFs are computed for every possible station pair and then stacked over 183 days. Finally, we reorder CCFs with hypocentral distance (interstation distance), as shown in Figure 7b. We apply the Fourier transform to CCFs to obtain the spectral CCFs. After getting the 1-day base stacked spectral CCF, we calculate the $I(\omega,c)$ in the $\omega - c$ domain by the F-J method using equation 13. The image of $I(\omega,c)$ is showed in Figure 7c. The appearance of overtones in the image is quite apparent in frequency range of 0.13–0.5 Hz, whereas the fundamental mode appears in frequencies below 0.3 Hz.

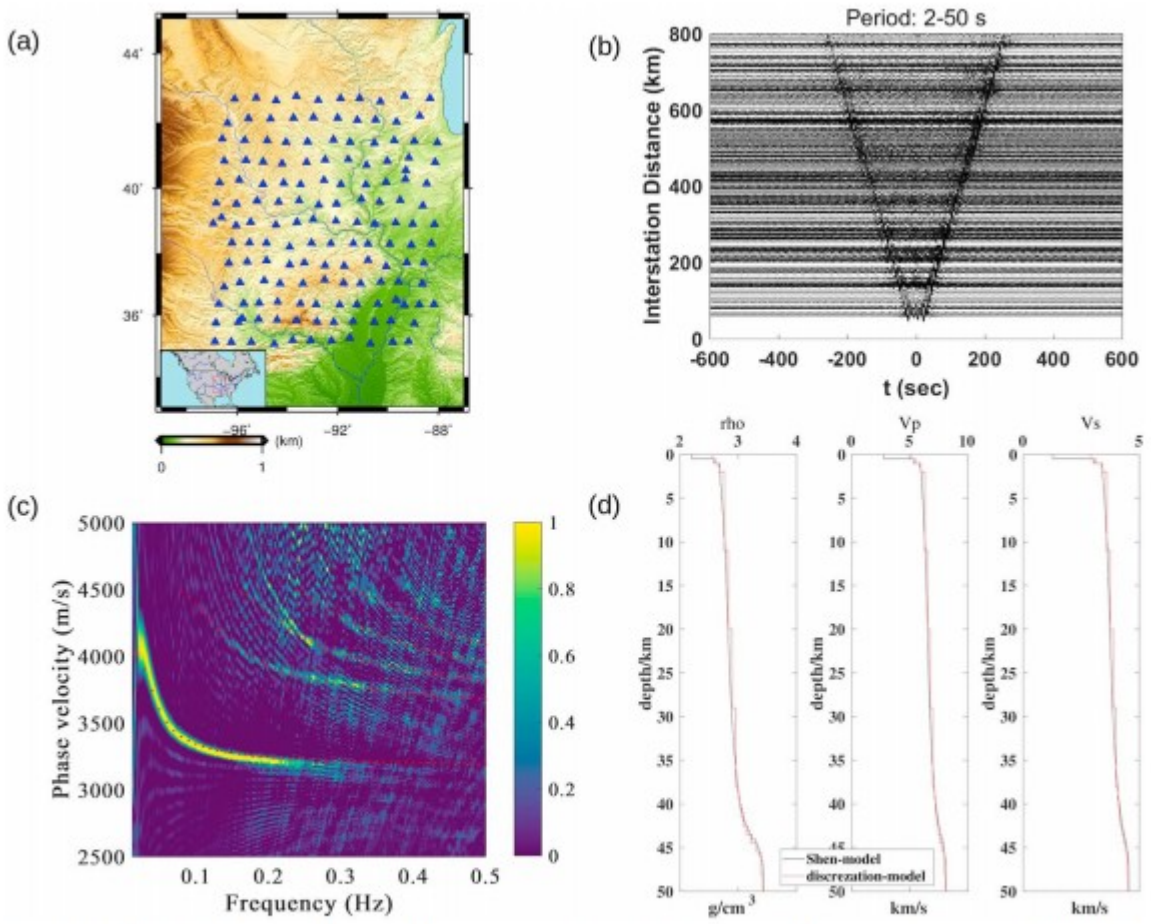

Figure 7. (a) Distribution map of the broadband seismographic stations used in this study. (b) Example of CCFs for station pairs in 2- to 20-s-period band. (c) The F-J spectrogram $I(\omega, c)$ estimated by the F-J method from ambient seismic noise data with theoretical dispersion curves. White solid lines denote the theoretical dispersion curves. (d) Average 1-D model in the study area.

To understand the $I(\omega,c)$ obtained by the F-J method, we calculate the theoretical dispersion curves of a one-dimensional velocity model beneath the observation array. The one-dimensional velocity model we used for this case is constructed by averaging the crustal velocity model of Shen and Ritzwoller (2016) beneath the area ranging from latitude 36° to 42° and longitude 96° to 90°, and depth down to 50 km. The averaged 1-D velocity is then discretized into 18 flat layers, as shown in Figure 7d. We calculate theoretical dispersion curves and project them onto the image of $I(\omega,c)$, as shown in Figure 7c. It can clearly be seen that the dispersion curves (thin, red dotted lines) of the fundamental, first higher, second higher, and third higher modes match the recognized “hot lines” (narrow area with larger values) on the F-J spectrogram $I(\omega,c)$ very well. The fundamental mode is clear below 0.25 Hz, blurred between 0.25 and 0.33 Hz and cannot be recognized above 0.33 Hz. The fourth-order and higher-mode dispersion curves are unclear.

As shown in Figure 8a, the second application to USArray data is located in further west of the previous investigated area, with latitude ranging from 36° to 44° and longitude from −104° to −96°. There are total 116 stations available in the study area, data were recorded from 1 June 2011 to 1 December 2011 with total 183 days. With the same procedure as described in the previous application to USArray data, we obtain the $I(\omega,c)$ image shown in Figure 8b.

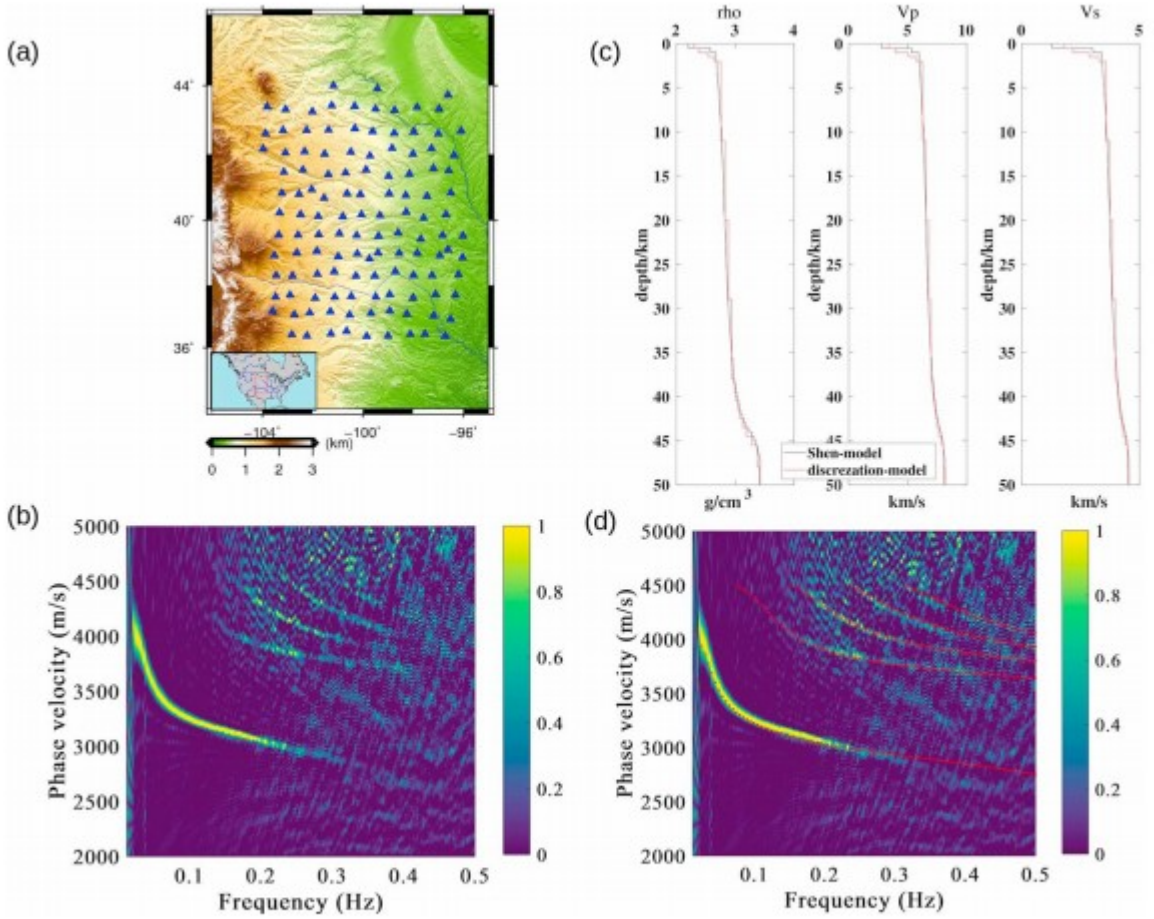

Figure 8. (a) Distribution map of the broadband seismographic stations used in this study. (b) The F-J spectrogram $I(\omega, c)$ estimated by the F-J method from ambient seismic noise data. (c) Average 1-D model in the study area. (d) The F-J spectrogram with theoretical dispersion curves. White solid lines denote the theoretical dispersion curves.

The dispersion curves of multimodes appear clearly in Figure 8b. The fundamental mode appears in frequency ranges of 0.02–0.35 Hz and the overtones appear in frequencies above 0.13 Hz. We also calculate the theoretical dispersion curves of a 1-D structure model beneath the observation array to understand the obtained $I(\omega,c)$ image. The local 1-D structure model used for calculating the theoretical dispersion curves, as shown in Figure 8c, is constructed by averaging the selected region (latitude 36° to 44°, longitude −100° to −104°) from Shen and Ritzwoller's (2016) model. The computed dispersion curves (red dotted lines) are projected onto

the $I(\omega,c)$ image shown in Figure 8d. It clearly shows that the dispersion curves of the fundamental, first higher, second higher, third higher, and even the fourth higher modes match the discernible dispersion curves on the $I(\omega,c)$ image. The fundamental dispersion curve is clear below 0.22 Hz but unclear between 0.22 and 0.34 Hz.

Although the dispersion curves from our $I(\omega,c)$ image agree quite well with theoretical dispersion curves of the current averaged structure models from Shen and Ritzwoller (2016), slight discrepancies are discernible. The F-J method assumes the survey region as a 1-D structure, which can be regarded as the complicated weighted average of the actual structure. The reference models are the horizontal average of 3-D structure of Shen and Ritzwoller (2016). It is reasonable that the two structures are slightly different as well as their corresponding dispersion curves. The approximation to Green's function (caused by the approximate satisfaction of the equipartition assumption of the ambient field), lateral variation, and anisotropy also decrease the quality of the $I(\omega,c)$ image.

5 Discussion

As seen in previous sections, although the overtones are clear and obvious in the $I(\omega,c)$ image generated by equation 13, there are some “noisy” images interfering the dispersion curves. These noisy images are mainly caused by the approximately evaluating of $I(\omega,c)$, namely, between the discrete summation and exact integral. According to the well-known Nyquist-Shannon theorem (Nyquist, 1928; Shannon, 1949), spatial sampling rate (Δr) should satisfy the following condition to avoid aliasing,

$$2k \le \frac{2\pi}{\Delta r}. \quad (14)$$

And resolution of the image in *f-k* domain is controlled by the maximum extent of the observation array,

$$\Delta k \le \frac{2\pi}{r_{\max}}. \quad (15)$$

To understand the cause of the noisy images, we use synthetic data to illustrate the effects of spatial sampling rate and the maximum extent of the observation array. For simplicity, instead of using the noise derived Green's function, we use the synthetic Green's function due to a vertical single force acting on the surface for model 1. We use the generalized reflectivity method (e.g., Chen, 1993, 1999; Chen & Zhang, 2001; Hisada, 1994; Kennett, 1986; Zhang et al., 2003) to calculate the synthetic seismograms, the observation array is a linear one, that is, all receivers locate along a straight line on the surface. Four arrays are considered as follows.

Array 1:interval of stations $\Delta r = 1$ m, extent of array $r_{\max} = 100$ m;

Array 2:interval of stations $\Delta r = 1$ m, extent of array $r_{\max} = 500$ m;

Array 3:interval of stations $\Delta r = 5$ m, extent of array $r_{\max} = 500$ m;

Array 4:interval of stations is random, extent of array $r_{max} = 500$ m, number of stations is 100.

Applying the F-J method to the synthetic seismograms of the three arrays, we obtain the images of $I(\omega,c)$ shown in Figure 9. Compared the images in top row with the ones in the second row of Figure 9, the resolution of the F-J spectrogram $I(\omega,c)$ obviously improved with the increase in extent of the array r_{max}. The resolution of high frequency is better than low frequency in *f-c* domain with same r_{max}. However, the resolution of the image in *f-k* domain is independent of frequency but is only controlled by r_{max} according equation 15. The frequency dependence in *f-c* domain is due to the conversion of *k* to *c*. Since $k = \frac{2\pi f}{c}$, we have $|\Delta c| = \frac{c^2}{2\pi f}|\Delta k|$. For low frequency, the uncertainty of phase velocity $|\Delta c|$ is amplified by a factor $\frac{c^2}{2\pi f}$, for lower frequencies, we find larger amplification.

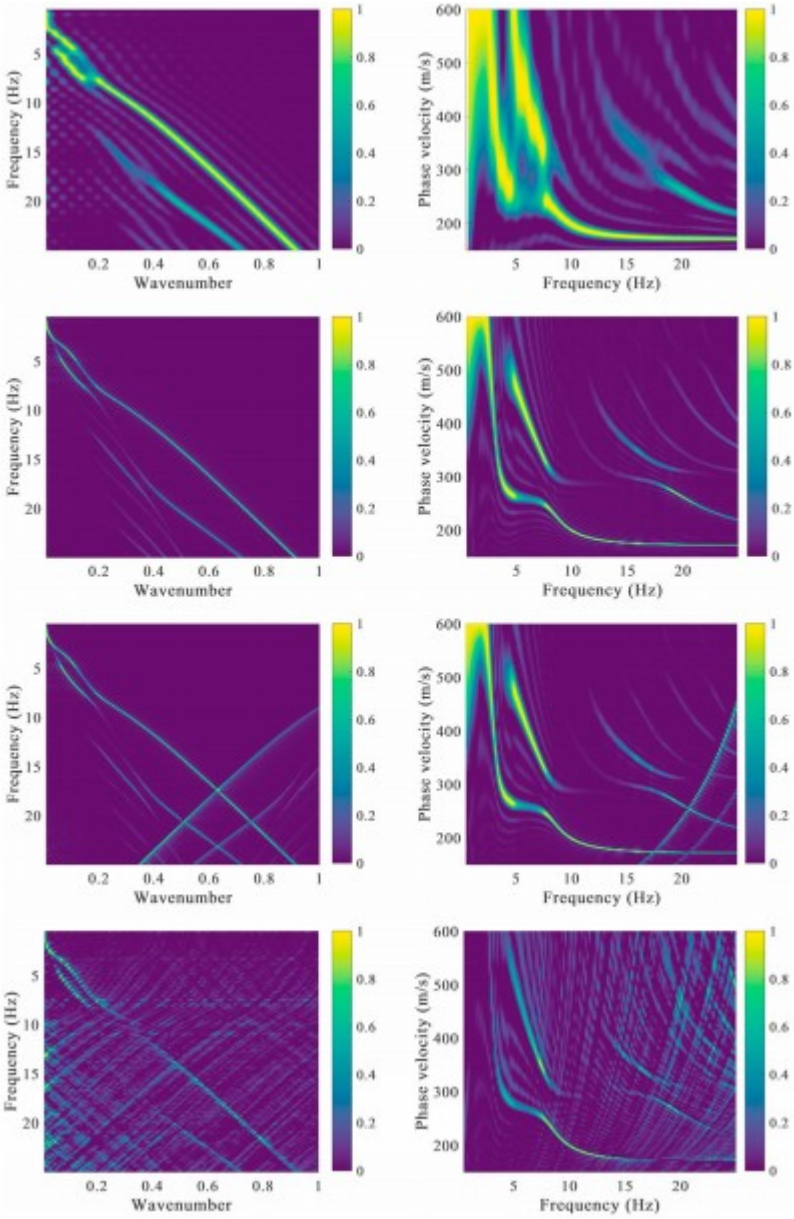

Figure 9. The F-J spectrograms from synthetic Green's function with different arrays. The left column are the F-J spectrograms in *f-k* domain. The right column are the F-J spectrograms in *f-c* domain. The top row is the ones of the array1 ($\Delta r = 1$ m, $r_{max} = 100$ m), the sencond row is the ones of the array2 ($\Delta r = 1$ m, $r_{max} = 500$ m), the third row is the ones of the array3 ($\Delta r = 5$ m, $r_{max} = 500$ m; the bottom is the ones of the array4 with the irregular interstation distance, $r_{max} = 500$ m).

In the third row of Figure 9, the streaks crossing over the theoretical dispersion curves are aliasing due to insufficient spatial sampling rate. The maximum wave number we could estimate from the $I(\omega,c)$ image is $k_{max} = 0.628$ m^{-1} according to equation 14. This exactly is what showed in the left panel of the bottom row in Figure 9, where the spurious curves crossing over those true dispersion curves are the extension of the images $I(\omega,c)$ in range of $k \in (-1,0)$. The right panel is just the conversion into *f-c* domain from the left image. The bottom row of Figure 9 are the $I(\omega,c)$ images of array 4. The

minimum interval is min(Δr) = 1.08 m, the maximum interval is max(Δr) = 16.24 m, the average interval is 5.07 m. This shows a same pattern as seen from Figures 7 and 8.

Aside from the effects of insufficient spatial sampling, there are other errors, such as the approximation to Green's function, laterally heterogenous variation, and lateral anisotropy. Although the theoretical basis for extracting Green's function from ambient seismic noise data is solid (e.g., Kimman & Trampert, 2010; Sanchezsesma & Campillo, 2006; Sato et al., 2012), the assumptions for this theory, such as ergodicity, equipartition, or other statistical assumptions are never fully satisfied in practice. In practice with field data studies, there is poor agreement with these assumptions, which adds to the noise in the final $I(\omega,c)$ image.

Another issue regarding the accuracy of the F-J method is the array pattern as shown in Figures 3 and 4. According to our numerical experiments, the array with randomly distributed geophones offers the best results under the same conditions in terms of total number of geophones (100) and array extent (200 m). In other words, the total raw data are the same for three arrays, but the results of the random array perform better than others. To understand this, we need to recall the basic formula we rely on. The key of F-J method is to calculate the F-J spectrogram $I(\omega,c)$ by using equation 13, which is an approximation to the exact $I(\omega,c)$, the frequency-Bessel transform of $\hat{C}(r,\omega)$. $I(\omega,c)$ is defined by an integral along hypocentral distance. Therefore, the quality or resolution of the $I(\omega,c)$ image depends on the degree of approximation of the finite discrete summation. With a better approximation to the summation a better image quality could be obtained.

To explain why does the random distribution array perform best, we plot the interstation distances $\{r_j\}$ distribution of all possible stations pairs of each array in Figure 10. The horizontal axis is r_j (j = 1,2,…), and the vertical axis of Figure 10a is the total number of all possible station pairs with same r_j. For example, in the linear array, intervals between nearest neighbor station are same and equal to 2 m; therefore, there are total 99 of $r_1 = 2$ m; similarly, there are 98 of $r_2 = 4$ m, … and 1 of $r_{99} = 200$ m, as shown as black dots in Figure 10a. In the same way, the distributions of distances between all possible station pairs r_j for other two arrays are plotted as red dots and blue dots in Figure 10. Theoretically, the number of all possible station pairs from a 100-station array is $C_{100}^2 = 4,950$. However, only 99 station pairs, r_j, are nondegenerate for linear array, while 517 and 4,723 are nondegenerate for the trilinear and random arrays, respectively, as shown in Figure 10b. Only those nondegenerate r_j can effectively be used to calculate the $I(\omega,c)$ image. For same integration extent, the more and smaller subintervals is, the more accurate the numerical integral $I(\omega,c)$ will be obtained. Therefore, the random array, with much more and finer subintervals, can produce better quality $I(\omega,c)$ as seen in Figure 4c.

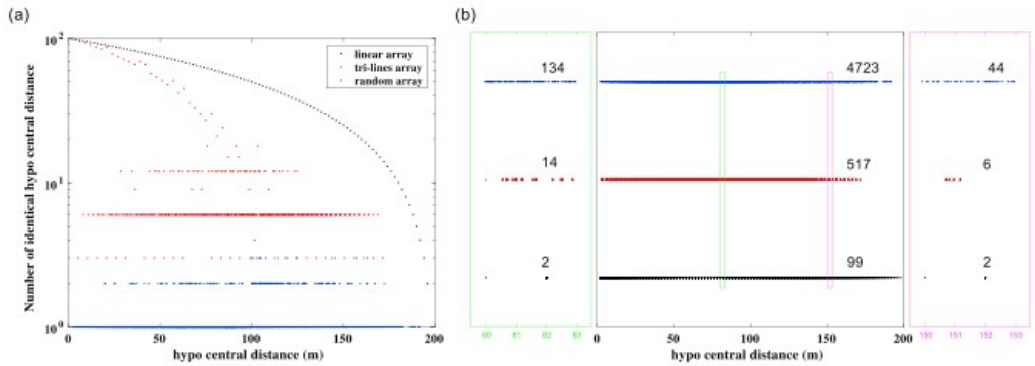

Figure 10. (a) Hypocentral distance r_j distribution of different observation array. Black dots, red dots, and blue dots are r_j of linear, trilines, and random observation array, respectively. (b) Projection map of hypocentral distrubution of different observation array onto the x axis. The left side and right side are the details of green and purple boxes. It indicates the number of valid hypocentral distance for integral.

6 Conclusions

In this study, we proposed a new ambient seismic noise analysis method called the frequency-Bessel transform method (F-J method), which can clearly image the dispersion curves of multimodes from ambient seismic noise data recorded by an observation array. By using synthetic data from given models, we systematically investigated on the validity and applicability of the F-J method. We applied this new method to process some ambient seismic noise data recorded by USArray and obtained clear dispersion curves of overtones in addition to the fundamental mode. Moreover, we analyzed the main factors affecting the resolution and accuracy of the results of the F-J method.

On the basis of studies presented in this paper, we draw the following conclusions.

1. The F-J method is a valid and applicable method for imaging the dispersion curves of the fundamental mode and overtones from ambient seismic noise data. It is an array analysis method and can be used for studies at different scales or frequencies.
2. The quality of dispersion curves extracted by the F-J method from ambient seismic noise data of an observational array depends on both the extent and the intervals between neighbor stations of the array. The larger the extent, the higher the resolution of results; the smaller the interval, the better the quality of results.
3. The distribution of seismographic stations (or receivers) of the observation array used in the F-J method is flexible and can be a linear or random pattern. Furthermore, under same other conditions, a data acquisition array with random distribution of receivers is the best suitable for applying the F-J method.
4. The preliminary applications to the ambient seismic noise data of USArray show that the F-J method is able to extract the dispersion

curves of the fundamental mode as well as several overtones from a real-field array data.

Acknowledgments

We acknowledge the IRIS for allowing us using the USArray data (We can get the USArray seismic data from website: https://ds.iris.edu/ds/nodes/dmc/data/types/waveform-data/). Finally, we acknowledge the financial support by the National Science Foundation of China (NSFC-41790465 and NSFC-41661134014).

Appendix A: Derivation of Equation (13) in the Text

As seen equation 6, only an approximate $I(\omega,c)$ can be obtained with the use of the available seismic data from the observation array. Here we show how to obtain an approximation $I(\omega,c)$ by using limited number of seismic data from available observation array.

First, we approximate the infinite integral in equation 6 by the following truncation.

$$\int_0^{+\infty} G(r)J_0(kr)r\,\mathrm{d}r \approx \sum_{j=1}^{N}\int_{r_{j-1}}^{r_j} G(r)J_0(kr)r\,\mathrm{d}r, \quad \text{(A1)}$$

where $0 = r_0 < r_1 < r_2 < \ldots < r_j < \ldots < r_N$.

Within each interval $[r_{j-1}, r_j]$, we can analytically evaluate the integral if integrand $G(r)$ can be approximated by a linear function of r. Therefore, we first approximate $G(r)$ by a linear function as follows:

$$G(r) \approx a_j + b_j r, \quad \text{(A2)}$$

with

$$a_j = G(r_{j-1}) - \left[\frac{G(r_j)-G(r_{j-1})}{r_j - r_{j-1}}\right] r_{j-1} \quad \text{and} \quad b_j = \frac{G(r_j)-G(r_{j-1})}{r_j - r_{j-1}}. \quad \text{(A3)}$$

Substituting equation A2 into equation A1, we have

$$\int_0^{+\infty} G(r)J_0(kr)r\,\mathrm{d}r \approx \sum_{j=1}^{N}\left\{ a_j \int_{r_{j-1}}^{r_j} rJ_0(kr)\,\mathrm{d}r + b_j \int_{r_{j-1}}^{r_j} r^2 J_0(kr)\,\mathrm{d}r \right\}. \quad \text{(A4)}$$

With recursive formulas of Bessel functions (e.g., Arfken et al., 2012), we can easily proof the following formulas:

$$\int xJ_0(x)\,\mathrm{d}x = xJ_1(x), \quad \text{(A5)}$$

$$\int x^2 J_0(x)\,\mathrm{d}x = x^2 J_1(x) + xJ_0(x) - \int J_0(x)\,\mathrm{d}x. \quad \text{(A6)}$$

Finally, substituting equations A5 and A6 into equation A4 yields

$$\int_0^{+\infty} G(r)J_0(kr)r\,\mathrm{d}r \approx \sum_{j=1}^{N}\left\{\frac{1}{k}G(r)rJ_1(kr)+\frac{b_j}{k^3}\left[krJ_0(kr)-B_0(kr)\right]\right\}\Bigg|_{r_{j-1}}^{r_j}, \quad \text{(A7)}$$

where $B_0(x)\equiv\int_0^x J_0(\eta)\,\mathrm{d}\eta$.

References

Aki, K. (1957). Space and time spectra of stationary stochastic waves, with special reference to microtremors. *Bulletin of the Earthquake Research Institute*, 35, 415– 456.

Arfken, G., Weber, H., & Harris, F. (2012). *Mathematical methods for physicists: A comprehensive guide 7th edn*. london: Academic Press.

Asten, M. W. (2006). Site shear velocity profile interpretation from microtremor array data by direct fitting of SPAC curves. In *Proceedings of the Third International Symposium on the Effects of Surface Geology on Seismic Motion (ESG2006)* (Vol. 1, p. 99) Citeseer.

Bensen, G. D., Ritzwoller, M. H., Barmin, M., Levshin, A. L., Lin, F. C., Moschetti, M. P., Shapiro, N. M., & Yang, Y. (2007). Processing seismic ambient noise data to obtain reliable broad-band surface wave dispersion measurements. *Geophysical Journal International*, 169(3), 1239– 1260.

Bensen, G. D., Ritzwoller, M. H., & Yang, Y. (2009). A 3-D shear velocity model of the crust and uppermost mantle beneath the united states from ambient seismic noise. *Geophysical Journal International*, 177(3), 1177– 1196.

Boaga, J., Cassiani, G., Strobbia, C., & Vignoli, G. (2013). Mode misidentification in Rayleigh waves: Ellipticity as a cause and a cure. *Geophysics*, 78(4), EN17-EN28.

Bonnefoy-Claudet, S., Cornou, C., Kristek, J., Ohrnberger, M., Wathelet, M., Bard, P.-Y., Moczo, P., Fäh, D., & Cotton, F. (2004). Simulation of seismic ambient noise: I. Results of H/V and array techniques on canonical models. In *Proc. 13th World Conf. on Earthquake Engineering* (p. 1120).

Brooks, L. A., Townend, J., Gerstoft, P., Bannister, S., & Carter, L. (2009). Fundamental and highermode rayleigh wave characteristics of ambient seismic noise in New Zealand. *Geophysical Research Letters*, 36, L23303. https://doi.org/10.1029/2009gl040434

Campillo, M., & Paul, A. (2003). Long-range correlations in the diffuse seismic coda. *Science*, 299(5606), 547– 549.

Capon, J. (1969). High-resolution frequency-wavenumber spectrum analysis. *Proceedings of the IEEE*, 57(8), 1408– 1418.

Chen, X. (1993). A systematic and efficient method of computing normal modes for multilayered half-space. *Geophysical Journal International*, 115(2), 391– 409.

Chen, X. (1999). Seismogram synthesis in multi-layered half-space Part I. Theoretical formulations. *Earthquake Research in China*, 13(2), 149– 174.

Chen, X.-f., & Zhang, H.-m. (2001). An efficient method for computing Green's functions for a layered half-space at large epicentral distances. *Bulletin of the Seismological Society of America*, 91(4), 858– 869.

De Nil, D. (2005). Characteristics of surface waves in media with significant vertical variations in elasto-dynamic properties. *Journal of Environmental and Engineering Geophysics*, 10(3), 263– 274.

Derode, A., Larose, E., Campillo, M., & Fink, M. (2003). How to estimate the greens function of a heterogeneous medium between two passive sensors? Application to acoustic waves. *Applied Physics Letters*, 83(15), 3054– 3056.

Foti, S., Lai, C. G., Rix, G. J., & Strobbia, C. (2014). *Surface wave methods for near-surface site characterization*. Boca Raton: CRC Press.

Gualtieri, L., Stutzmann, E., Capdeville, Y., Farra, V., Mangeney, A., & Morelli, A. (2015). On the shaping factors of the secondary microseismic wavefield. *Journal of Geophysical Research: Solid Earth*, 120, 6241– 6262. https://doi.org/10.1002/2015JB012157

Harmon, N., Forsyth, D. W., & Webb, S. C. (2007). Using ambient seismic noise to determine short-period phase velocities and shallow shear velocities in young oceanic lithosphere. *Bulletin of the Seismological Society of America*, 97(6), 2009– 2023.

Hisada, Y. (1994). An efficient method for computing Green's functions for a layered half-space with sources and receivers at close depths. *Bulletin of the Seismological Society of America*, 84(5), 1456– 1472.

Ikeda, T., Matsuoka, T., Tsuji, T., & Hayashi, K. (2012). Multimode inversion with amplitude response of surface waves in the spatial autocorrelation method. *Geophysical Journal International*, 190(1), 541– 552.

Jacobson, M. J. (1962). Space-time correlation in spherical and circular noise fields. *The Journal of the Acoustical Society of America*, 34(7), 971– 978.

Kennett, B. (1986). Seismic wave propagation in stratified media. *Geophysical Journal of the Royal Astronomical Society*, 86(1), 219– 220.

Kimman, W. P., & Trampert, J. (2010). Approximations in seismic interferometry and their effects on surface waves. *Geophysical Journal International*, 182(1), 461– 476.

Lacoss, R. T., Kelly, E. J., & Toksöz, M. N. (1969). Estimation of seismic noise structure using arrays. *Geophysics*, 34(1), 21– 38.

Lin, F. C., Li, D., Clayton, R. W., & Hollis, D. (2013). High-resolution 3D shallow crustal structure in Long Beach, California: Application of ambient noise tomography on a dense seismic array. *Geophysics*, 78(4), Q45– Q56.

Lin, F. C., Moschetti, M. P., & Ritzwoller, M. H. (2008). Surface wave tomography of the western United States from ambient seismic noise: Rayleigh and love wave phase velocity maps. *Geophysical Journal International*, 173(1), 281– 298.

Lin, F. C., Ritzwoller, M. H., & Shen, W. (2011). On the reliability of attenuation measurements from ambient noise cross-correlations. *Geophysical Research Letters*, 38, L11303. https://doi.org/10.1029/2011GL047366

Lobkis, O. I., & Weaver, R. L. (2001). On the emergence of the Green's function in the correlations of a diffuse field. *The Journal of the Acoustical Society of America*, 110(6), 3011– 3017.

Luco, J. E., & Apsel, R. J. (1983). On the Green's functions for a layered half-space. Part I. *Bulletin of the Seismological Society of America*, 73(4), 909– 929.

Luo, Y., Xu, Y., Liu, Q., & Xia, J. (2008). Rayleigh-wave dispersive energy imaging and mode separating by high-resolution linear Radon transform. *The Leading Edge*, 27(11), 1536– 1542.

Malischewsky, P. G., Scherbaum, F., Lomnitz, C., Tuan, T. T., Wuttke, F., & Shamir, G. (2008). The domain of existence of prograde Rayleigh-wave particle motion for simple models. *Wave Motion*, 45(4), 556– 564.

Maraschini, M., Ernst, F., Foti, S., & Socco, L. (2010). A new misfit function for multimodal inversion of surface waves. *Geophysics*, 75(4), G31– G43.

McMechan, G. A., & Yedlin, M. J. (1981). Analysis of dispersive waves by wave field transformation. *Geophysics*, 46(6), 869– 874.

Mordret, A., Landes, M., Shapiro, N. M., Singh, S. C., & Roux, P. (2014). Ambient noise surface wave tomography to determine the shallow shear velocity structure at Valhall: Depth inversion with a neighbourhood algorithm. *Geophysical Journal International*, 198(3), 1514– 1525.

Moschetti, M., Ritzwoller, M., & Shapiro, N. (2007). Surface wave tomography of the western United States from ambient seismic noise: Rayleigh wave group velocity maps. *Geochemistry, Geophysics, Geosystems*, 8, Q08010. https://doi.org/10.1029/2007GC001655

Nakamura, Y. (1989). A method for dynamic characteristics estimation of subsurface using microtremor on the ground surface. *Quarterly Report of Rtri*, 30(1), 25– 33.

Nishida, K., Kawakatsu, H., & Obara, K. (2008). Threedimensional crustal S wave velocity structure in Japan using microseismic data recorded by Hi-net tiltmeters. *Journal of Geophysical Research*, 113, B10302. https://doi.org/10.1029/2007JB005395

Nishida, K., Montagner, J.-P., & Kawakatsu, H. (2009). Global surface wave tomography using seismic hum. *Science*, 326(5949), 112– 112.

Nolet, G., & Panza, G. F. (1976). Array analysis of seismic surface waves: Limits and possibilities. *Pure and Applied Geophysics*, 114(5), 775– 790.

Nyquist, H. (1928). Certain topics in telegraph transmission theory. *Transactions of the American Institute of Electrical Engineers*, 47(2), 617– 644.

Okada, H., & Suto, K. (2003). *The microtremor survey method*, vol. 12. Tulsa, OK: Society of Exploration Geophysicists with the cooperation of Society of Exploration Geophysicists of Japan [and] Australian Society of Exploration Geophysicists.

Pan, Y., Xia, J., Xu, Y., Xu, Z., Cheng, F., Xu, H., & Gao, L. (2016). Delineating shallow S-wave velocity structure using multiple ambient-noise surface-wave methods: An example from western Junggar, China. *Bulletin of the Seismological Society of America*, 106(2), 327– 336.

Park, C. B., & Miller, R. D. (2008). Roadside passive multichannel analysis of surface waves (MASW). *Journal of Environmental and Engineering Geophysics*, 13(1), 1– 11.

Park, C. B., Miller, R. D., & Xia, J. (1998). Imaging dispersion curves of surface waves on multi-channel record. In *SEG Technical Program Expanded Abstracts 1998*, Society of Exploration Geophysicists, pp. 1377– 1380.

Park, C. B., Miller, R. D., Xia, J., & Ivanov, J. (2007). Multichannel analysis of surface waves (MASW)—Active and passive methods. *Geophysics*, 26(1), 60– 64.

Prieto, G. A., Denolle, M. A., Lawrence, J. F., & Beroza, G. C. (2011). On amplitude information carried by the ambient seismic field. *Comptes Rendus Geoscience*, 343(343), 600– 614.

Rivet, D., Campillo, M., Sanchezsesma, F. J., Shapiro, N. M., & Singh, S. K. (2015). Identification of surface wave higher modes using a methodology based on seismic noise and coda waves. *Geophysical Journal International*, 203(2), 856– 868.

Sabra, K. G., Gerstoft, P., Roux, P., Kuperman, W., & Fehler, M. C. (2005a). Extracting time-domain Green's function estimates from ambient seismic noise. *Geophysical Research Letters*, 32, L03310. https://doi.org/10.1029/2004GL021862

Sabra, K. G., Gerstoft, P., Roux, P., Kuperman, W., & Fehler, M. C. (2005b). Surface wave tomography from microseisms in Southern California. *Geophysical Research Letters*, 32, L14311. https://doi.org/10.1029/2005GL023155

Sánchez-Sesma, F. J., Rodríguez, M., Iturrarán-Viveros, U., Luzón, F., Campillo, M., Margerin, L., García-Jerez, A., Suarez, M., Santoyo, M. A., & Rodríguez-Castellanos, A. (2011). A theory for microtremor H/V spectral ratio:

Application for a layered medium. *Geophysical Journal International*, 186(1), 221– 225.

Sanchezsesma, F. J., & Campillo, M. (2006). Retrieval of the greens function from cross correlation: The canonical elastic problem. *Bulletin of the Seismological Society of America*, 96(3), 1182– 1191.

Sato, H., Fehler, M. C., & Maeda, T. (2012). Green's function retrieval from the cross-correlation function of random waves, *Seismic wave propagation and scattering in the heterogeneous Earth: Second edition* pp. 401– 450). Berlin, Heidelberg: Springer.

Satoh, T., Kawase, H., Iwata, T., Higashi, S., Sato, T., Irikura, K., & Huang, H. (2001). S-wave velocity structure of the Taichung Basin, Taiwan, estimated from array and single-station records of microtremors. *Bulletin of the Seismological Society of America*, 91(5), 1267– 1282.

Savage, M. K., Lin, F. C., & Townend, J. (2013). Ambient noise cross-correlation observations of fundamental and higher-mode Rayleigh wave propagation governed by basement resonance. *Geophysical Research Letters*, 40, 3556– 3561. https://doi.org/10.1002/grl.50678

Shannon, C. E. (1949). Communication in the presence of noise. *Proceedings of the IRE*, 37(1), 10– 21.

Shapiro, N. M., & Campillo, M. (2004). Emergence of broadband Rayleigh waves from correlations of the ambient seismic noise. *Geophysical Research Letters*, 31, L07614. https://doi.org/10.1029/2004GL019491

Shapiro, N. M., Campillo, M., Stehly, L., & Ritzwoller, M. H. (2005). High-resolution surface-wave tomography from ambient seismic noise. *Science*, 307(5715), 1615– 1618.

Shen, W., & Ritzwoller, M. H. (2016). Crustal and uppermost mantle structure beneath the United States. *Journal of Geophysical Research: Solid Earth*, 121, 4306– 4342. https://doi.org/10.1002/2016JB012887

Snieder, R. (2004). Extracting the Green's function from the correlation of coda waves: A derivation based on stationary phase. *Physical Review E*, 69(4), 046610.

Taylor, S. R., Gerstoft, P., & Fehler, M. (2009). Estimating site amplification factors from ambient noise. *Geophysical Research Letters*, 36, L09303. https://doi.org/10.1029/2009GL037838

Temme, N. M. (1996). Special functions: An introduction to the classical functions of mathematical physics. *American Journal of Physics*, 65(5), 452– 453.

Tian, Y., Shen, W., & Ritzwoller, M. H. (2013). Crustal and uppermost mantle shear velocity structure adjacent to the Juan de Fuca Ridge from ambient seismic noise. *Geochemistry Geophysics Geosystems*, 14, 3221– 3233. https://doi.org/10.1002/ggge.20206

Tokimatsu, K. (1997). Geotechnical site characterization using surface waves. In *Earthq. Geotech. Eng., Proc. IS-Tokyo'95 First Int. Conf. Earthq. Geotech. Eng., Balkema, Rotterdam*, pp. 1333– 1368.

Tomar, G., Stutzmann, E., Mordret, A., Montagner, J., Singh, S. C., & Shapiro, N. M. (2018). Joint inversion of the first overtone and fundamental mode for deep imaging at the Valhall oil field using ambient noise. *Geophysical Journal International*, 214(1), 122– 132.

Tuan, T. T., Scherbaum, F., & Malischewsky, P. G. (2011). On the relationship of peaks and troughs of the ellipticity (H/V) of Rayleigh waves and the transmission response of single layer over halfspace models. *Geophysical Journal International*, 184(2), 793– 800.

Wiggins, R. A. (1972). The general linear inverse problem—Implication of surface waves and free oscillations for Earth structure. *Reviews of Geophysics*, 10(1), 251– 285.

Yang, Y., & Ritzwoller, M. H. (2008). Characteristics of ambient seismic noise as a source for surface wave tomography. *Geochemistry Geophysics Geosystems*, 9, Q02008. https://doi.org/10.1029/2007GC001814

Yang, Y., Ritzwoller, M. H., Levshin, A. L., & Shapiro, N. M. (2007). Ambient noise Rayleigh wave tomography across Europe. *Geophysical Journal International*, 168(1), 259– 274.

Yang, Y., Shen, W., & Ritzwoller, M. H. (2011). Surface wave tomography on a large-scale seismic array combining ambient noise and teleseismic earthquake data. *Earthquake Science*, 24(1), 55– 64.

Yao, H., Gouedard, P., Collins, J. A., Mcguire, J. J., & Der Hilst, R. D. V. (2011). Structure of young East Pacific Rise lithosphere from ambient noise correlation analysis of fundamental- and higher-mode Scholte-Rayleigh waves. *Comptes Rendus Geoscience*, 343(8), 571– 583.

Yao, H., van Der Hilst, R. D., & De Hoop, M. V. (2006). Surface-wave array tomography in SE Tibet from ambient seismic noise and two-station analysis —I. Phase velocity maps. *Geophysical Journal International*, 166(2), 732– 744.

Yokoi, T. (2010). New formulas derived from seismic interferometry to simulate phase velocity estimates from correlation methods using microtremor. *Geophysics*, 75(4), SA71– SA83.

Zhang, S. X., & Chan, L. S. (2003). Possible effects of misidentified mode number on Rayleigh wave inversion. *Journal of Applied Geophysics*, 53(1), 17– 29.

Zhang, H.-m., Chen, X.-f., & Chang, S. (2003). An efficient numerical method for computing synthetic seismograms for a layered half-space with sources and receivers at close or same depths. *Pure and Applied Geophysics*, 160, 467– 486.

Zhang, B., & Lu, L. (2003). Guided waves in a stratified half-space. *Acoustical Physics*, 49(4), 420– 430.

Zhang, K., Zhang, B.-W., Liu, J.-X., & Xu, M. (2016). Analysis on the cross of Rayleigh-wave dispersion curves in viscoelastic layered media. *Chinese Journal of Geophysics (in Chinese)*, 59(3), 972– 980.